

# Facile Dry Coating Method of High-Nickel Cathode Material by Nanostructured Fumed Alumina ( $\text{Al}_2\text{O}_3$ ) Improving the Performance of Lithium-Ion Batteries

Marcel J. Herzog, Nicolas Gauquelin, Daniel Esken, Johan Verbeeck, and Jürgen Janek\*

Surface coating is a crucial method to mitigate the aging problem of high-Ni cathode active materials (CAMs). By avoiding the direct contact of the CAM and the electrolyte, side reactions are hindered. Commonly used techniques like wet or ALD coating are time consuming and costly. Therefore, a more cost-effective coating technique is desirable. Herein, a facile and fast dry powder coating process for CAMs with nanostructured fumed metal oxides are reported. As the model case, the coating of high-Ni NMC ( $\text{LiNi}_{0.7}\text{Mn}_{0.15}\text{Co}_{0.15}\text{O}_2$ ) by nanostructured fumed  $\text{Al}_2\text{O}_3$  is investigated. A high coverage of the CAM surface with an almost continuous coating layer is achieved, still showing some porosity. Electrochemical evaluation shows a significant increase in capacity retention, cycle life and rate performance of the coated NMC material. The coating layer protects the surface of the CAM successfully and prevents side reactions, resulting in reduced solid electrolyte interface (SEI) formation and charge transfer impedance during cycling. A mechanism on how the coating layer enhances the cycling performance is hypothesized. The stable coating layer effectively prevents crack formation and particle disintegration of the NMC. In depth analysis indicates partial formation of  $\text{Li}_x\text{Al}_2\text{O}_3/\text{LiAlO}_2$  in the coating layer during cycling, enhancing lithium ion diffusivity and thus, also the rate performance.

service life, as well as to reduce costs.<sup>[1–3]</sup> Among all available cathode materials, high-nickel NMC ( $\text{LiNi}_x\text{Mn}_y\text{Co}_z\text{O}_2$  with  $x + y + z = 1$  and  $x > 0.5$ ) is one of the most promising candidates to meet these requirements.<sup>[4]</sup> The high-nickel content provides a higher specific capacity and relatively lower costs in comparison with cobalt-rich materials.<sup>[2,5,6]</sup>

A major general problem with layered cathode materials is still the aging and thus the loss of performance during cycling. This phenomenon is especially relevant for high-nickel NMC.<sup>[4]</sup> During cycling the NMC materials suffer from several electrochemical degradation. Surface transformations such as the formation of a NiO-like phase due to the reduction of  $\text{Ni}^{4+}$  in a highly delithiated state and oxygen loss as well as transition metal rearrangement destabilize the crystal structure.<sup>[6–12]</sup> This phase transition and also the volume change during (de)lithiation are supposed to initiate cracks in the cathode particles and lead to subsequent particle disintegration.<sup>[7,13,14]</sup>

In addition, the liquid electrolyte decomposes at the reactive surface of high-nickel NMC and electrolyte decomposition products deposit at the interface, leading to an increased resistance.<sup>[2,15–17]</sup> Furthermore, the conducting salt  $\text{LiPF}_6$ , which is commonly used in liquid electrolytes, reacts with trace amounts of  $\text{H}_2\text{O}$ , in all commercial cell components, to form hydrogen fluoride (HF).<sup>[18]</sup> The formed HF causes lattice distortion in the cathode material by dissolution of transition metal

## 1. Introduction

For the upscaling of state-of-the-art lithium-ion battery (LIB) technology from consumer electronics to large format cells for grid energy storage or electric vehicles, further development of active and inactive materials is still essential. The rising demand for high-performance LIBs necessitates to increase the energy density, power density, thermal stability, safety, and

M. J. Herzog, Prof. J. Janek  
Institute of Physical Chemistry and Center for Materials Research  
Justus-Liebig-University Giessen  
Heinrich-Buff-Ring 17, Giessen 35392, Germany  
E-mail: juergen.janek@phys.chemie.uni-giessen.de

 The ORCID identification number(s) for the author(s) of this article can be found under <https://doi.org/10.1002/ente.202100028>.

© 2021 The Authors. Energy Technology published by Wiley-VCH GmbH. This is an open access article under the terms of the Creative Commons Attribution-NonCommercial-NoDerivs License, which permits use and distribution in any medium, provided the original work is properly cited, the use is non-commercial and no modifications or adaptations are made.

DOI: 10.1002/ente.202100028

Dr. N. Gauquelin, Prof. J. Verbeeck  
Electron Microscopy for Materials Science  
University of Antwerp  
Campus Groenenborger, Groenenborgerlaan 171, Antwerpen 2020, Belgium

Dr. N. Gauquelin, Prof. J. Verbeeck  
NANOLab Center of Excellence  
University of Antwerp  
Groenenborgerlaan 171, Antwerpen 2020, Belgium

M. J. Herzog, Dr. D. Esken  
Evonik Operations GmbH  
Rodenbacher Chaussee 4, Hanau-Wolfgang 63457, Germany

ions out of the surface of the cathode material into the electrolyte.<sup>[3,15,19,20]</sup> All of these degradation mechanisms result in a decrease in capacity, performance, and cycle life.<sup>[2,3,14–17,19–21]</sup>

Surface coating has proven to be a very effective method to mitigate this aging problem by suppressing the direct contact between the active materials' surfaces and the liquid electrolyte.<sup>[4,7,15,22,23]</sup> A beneficial side effect of a stable coating layer is the improved storage property of high-nickel materials by keeping off CO<sub>2</sub> and H<sub>2</sub>O.<sup>[24,25]</sup> High-nickel materials tend to form surface impurities at ambient conditions, mostly carbonates, resulting in an enhanced capacity fading, increase in impedance, and gas generation during cycling.<sup>[26,27]</sup>

Apart from metal phosphates,<sup>[28,29]</sup> metal fluorides,<sup>[30–34]</sup> active electrode materials,<sup>[35–37]</sup> and carbon,<sup>[38–40]</sup> the most commonly used materials for the modification of cathode material surfaces are a vast variety of metal oxides, e.g., SiO<sub>2</sub>,<sup>[41]</sup> Al<sub>2</sub>O<sub>3</sub>,<sup>[42,43]</sup> TiO<sub>2</sub>,<sup>[44]</sup> V<sub>2</sub>O<sub>5</sub>,<sup>[17]</sup> ZrO<sub>2</sub>,<sup>[42,45]</sup> ZnO,<sup>[46]</sup> MgO,<sup>[42]</sup> Co<sub>3</sub>O<sub>4</sub>,<sup>[47]</sup> CeO<sub>2</sub>,<sup>[48]</sup> and so on. Among these Al<sub>2</sub>O<sub>3</sub> is the most established coating material. For example, Mohanty et al.<sup>[13]</sup> could significantly preserve the surface of NMC 811 (LiNi<sub>0.8</sub>Mn<sub>0.1</sub>Co<sub>0.1</sub>O<sub>2</sub>; ratio between nickel, manganese and cobalt = 8:1:1) particles by applying a 10 nm Al<sub>2</sub>O<sub>3</sub> coating layer. The cycling performance was significantly enhanced and the impedance decreased. No cracking and particle disintegration were observed. In addition, Al<sub>2</sub>O<sub>3</sub> acts as a very efficient HF scavenger.<sup>[49–51]</sup>

Commonly used methods for applying coatings on cathode materials are wet chemical,<sup>[17,41,48,52]</sup> sol–gel,<sup>[43,45]</sup> and atomic layer deposition (ALD) coating.<sup>[42,46,53]</sup> However, solvent-based coating approaches have recently become less favored because they require subsequent heating and drying steps, which cause additional energy costs.<sup>[25]</sup> In addition, the utilization of organic solvents is accompanied by environmental concerns over the resulting waste streams and possible volatile organic compound emissions.<sup>[54]</sup> The alternative ALD technology provides thin films with excellent conformity, leading to uniform coatings over morphologically complex surfaces,<sup>[55]</sup> but has disadvantages of low throughput and expensive running costs due to a low formation rate of the coating layer and expensive reactants.<sup>[56]</sup> Thus, the ALD process is considered critically for large-scale industrial production.<sup>[12]</sup>

A less investigated coating technique for cathode active materials (CAMs) is the dry particle coating approach.<sup>[25,47,57]</sup> During this process larger core particles (micron-sized) are coated directly with fine submicron-sized particles (coating material)

by mechanical forces without using any solvents and binders.<sup>[54,58,59]</sup> As the size of the coating material particles is very small, van der Waals or electrostatic interactions and the mechanical forces applied by the coating process keep them firmly attached to the larger core particles.<sup>[54,60–62]</sup> It does not involve harmful solvents and subsequent drying, resulting in substantial energy, cost, and time savings. This makes dry particle coating a very promising economically efficient and environmentally friendly method for surface modification.<sup>[62]</sup> Zheng et al.<sup>[63]</sup> recently published a dry mechanofusion coating process of NMC 622 with nano-Al<sub>2</sub>O<sub>3</sub>. By this process, a nonporous Al<sub>2</sub>O<sub>3</sub> coating layer was achieved that was retained during slurry making and improved LIB cathode cycling performance.

In this article we demonstrate a quite different dry coating approach of NMC701515 with a fumed nanostructured Al<sub>2</sub>O<sub>3</sub> by using a fast and simple process in a high energy mixer. By using the high energy mixer, the mixing time can be reduced significantly compared with the mechanofusion system, approximately by a factor of 4 from about 30 to 7 min.<sup>[63]</sup> In contrast to Zheng et al.<sup>[63]</sup> we achieve a porous coating layer, showing a reduced impedance, which is also very robust and durable. The fumed nanostructured Al<sub>2</sub>O<sub>3</sub> coating layer remains on the surface, without subsequent annealing, and protects the cathode particles successfully. Electrochemical evaluation of optimized coatings shows a significant enhancement in rate performance and capacity retention by the optimal amount of coating material, while the solid electrolyte interface (SEI) and charge transfer impedance is decreased. At the end, we elucidate the mechanism of the stabilization of the cathode material by the Al<sub>2</sub>O<sub>3</sub> coating by analyzing cycled electrodes.

The significant improvement of cathode cycling performance with a low amount of inactive coating material and the easy upscalability to large scale high intensity mixers makes our dry coating approach a highly promising process for commercialization in industrial manufacturing. This process is also easily transferable to other cathode materials and coating materials.

## 2. Results and Discussion

### 2.1. Dry Coating Process

The principle of our dry coating process of cathode materials using fumed nanostructured metal oxides is shown in **Figure 1**. Micron-sized NMC particles are acting as core particles (host

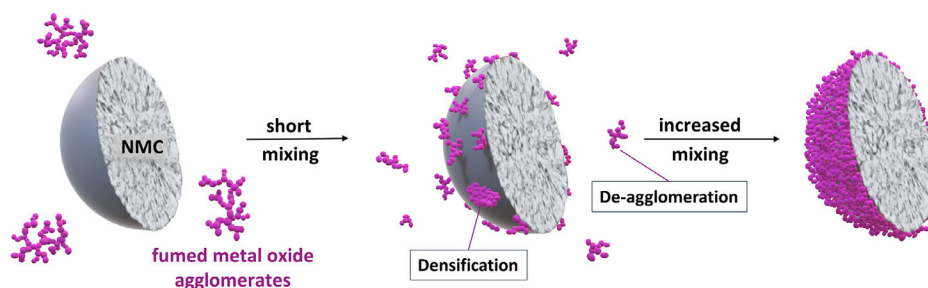


**Figure 1.** Schematic mechanism of the dry coating process in this study (cross-sectional view). The nanostructured fumed metal oxide is deagglomerated into smaller aggregates during the high energy mixing process and interacts with the surface of the cathode powder. This deagglomeration of the fumed metal oxide powder is the key of our dry coating method. After appropriate mixing, a continuous and strongly adhesive coating layer is formed.

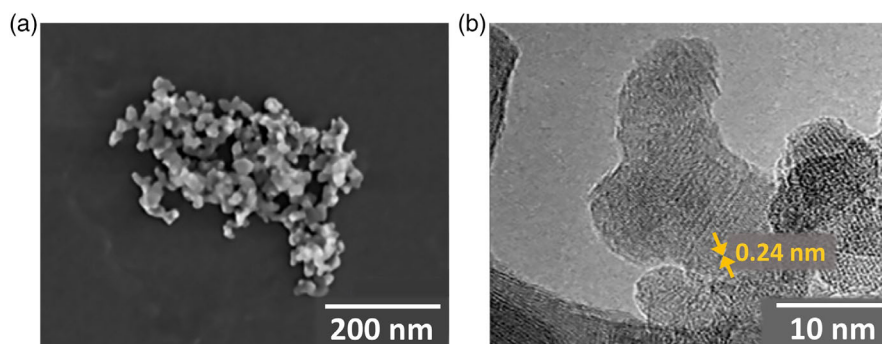


**Figure 2.** a) SEM image of fumed  $\text{Al}_2\text{O}_3$  single aggregate and b) HRTEM image of fumed  $\text{Al}_2\text{O}_3$ , showing that the material is crystalline, having the  $\gamma\text{-Al}_2\text{O}_3$  structure with a lattice distance of 0.24 nm.

particles) and the submicron-sized metal oxides as coating material (guest particles).

The fumed metal oxides are produced by flame hydrolysis and consist of agglomerated particles, having very high Brunauer–Emmett–Teller (BET) surfaces (fumed  $\text{Al}_2\text{O}_3$ :  $130\text{ m}^2\text{ g}^{-1}$ ).<sup>[64]</sup> **Figure 2a** shows a scanning electron microscopy (SEM) image of a fumed  $\text{Al}_2\text{O}_3$  single aggregate. A high-resolution transmission electron microscopy (HRTEM) image is shown in **Figure 2b**. The material is crystalline, having the  $\gamma\text{-Al}_2\text{O}_3$  structure with a lattice distance of 0.24 nm. The larger agglomerates can be split into smaller aggregates, which are built of nuclei formed in the flame, followed by growth processes (primary particle size of  $\approx 12\text{ nm}$ ), that are chemically bonded together to form highly nanostructured 3D entities with a more or less high degree of branching.<sup>[64]</sup> These aggregates cannot easily be split into individual primary particles.<sup>[64]</sup>

During the high energy mixing process, the nanostructured alumina is deagglomerated into smaller aggregates and starts to interact with the surface of the cathode powder. This deagglomeration of the fumed metal oxide powder is the key step of our dry coating method. The small nanostructured aggregate size provides high specific surface area and good adhesion to the CAM particle surfaces. The coating layer consists of 3D nanostructured aggregates of different sizes with a specific branching and not of spherical uniform nanoparticles. At a given mixing energy, a certain degree of densification and coalescence of the aggregates at the cathode particle surfaces is achieved, resulting in a quite continuous and strongly adhesive coating layer. The strong attachment to the surface of the CAM is attributed to physical interactions only. The coalescence and interlocking of the fumed aggregates may contribute to the strong adhesion of the coating layer to the surface. There is no need for an additional calcination step after dry coating for fixing the fumed metal oxide particles. Apart from energy savings this is an additional advantage for the cycling stability. Han et al.<sup>[65]</sup> found that annealing of an  $\text{Al}_2\text{O}_3$ -coated high-nickel NMC leads to the diffusion of Al into the bulk phase. This was found to be detrimental to the protection function of surface coatings, leading to poor overall cyclability.<sup>[65]</sup> The negative effect of annealing fumed  $\text{Al}_2\text{O}_3$ -coated NMC on the cycling behavior is further confirmed by testing an annealed sample later in this article.

Due to the strong forces applied to the materials at the high rotating speed of the rotor, very short processing times (6 min) are required to achieve the coating. The mixing intensity and time are crucial for this dry coating process. Under a too low mixing intensity or a too low mixing time, the energy is not sufficient to break up the agglomerates, resulting in an incomplete coverage of NMC surfaces and larger  $\text{Al}_2\text{O}_3$  agglomerates, which are not on the surface but present next to the cathode particles due to insufficient impact force. If the mixing intensity is too high, breakage of the secondary particle structure of the CAM can occur.

## 2.2. Analysis of Coated Cathode Material

### 2.2.1. Influence of Coating Process on Host Cathode Material

The particle size distribution (PSD) of the uncoated NMC701515 and the  $\text{Al}_2\text{O}_3$ -coated NMC is compared in **Figure 3** and shows a nearly identical distribution. This demonstrates that the NMC particles stay intact after exposure to the high shear forces during the mixing process and do not break into smaller pieces. The measured particle size for the uncoated NMC is slightly lower ( $D_{50} = 10.63\ \mu\text{m}$ ) than for the coated ones ( $D_{50} = 10.78\ \mu\text{m}$ ), which is reasonable because we are coating material on top of the surface.

The X-ray powder diffraction (XRD) patterns of the NMC coated by 1 wt%  $\text{Al}_2\text{O}_3$  (see **Figure S1a**, Supporting Information) and the pristine NMC material (**Figure S1b**, Supporting Information) are shown in **Figure S1**, Supporting Information.

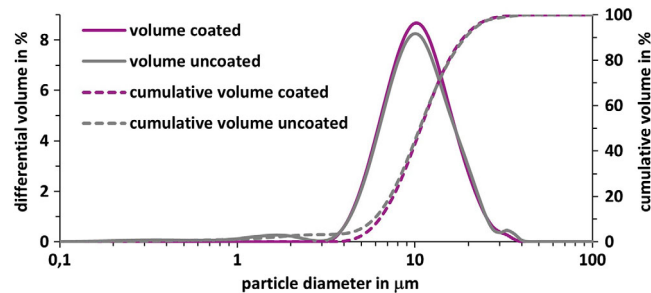


**Figure 3.** Volume-based PSD of uncoated NMC701515 and NMC701515 coated by 1 wt% fumed  $\text{Al}_2\text{O}_3$ .

Information. All diffraction peaks are indexed on the basis of the  $\alpha$ -NaFeO<sub>2</sub> structure with a space group of R-3 m. No difference in the XRD signals of coated and uncoated NMC was observed, indicating that the coating process is not influencing the original bulk crystal structure of the cathode material. No extra diffraction peaks of the thin coating layer are detected.

### 2.2.2. Characterization of the Coating Layer

The coated and uncoated NMC materials were investigated by SEM in combination with energy dispersive X-ray spectroscopy (SEM-EDX). In the elemental mapping of NMC dry coated by 1 wt% Al<sub>2</sub>O<sub>3</sub>, a fully and homogeneous coverage around all cathode particles was found as indicated by the aluminum signal (Figure 4a,b). No large Al<sub>2</sub>O<sub>3</sub> agglomerates were detected, showing that deagglomeration of nanostructured fumed Al<sub>2</sub>O<sub>3</sub> was successful. In addition, no free unattached Al<sub>2</sub>O<sub>3</sub> next to the cathode particles was found, indicating the strong adhesion between coating and substrate. The comparison of the BSE images of the coated (Figure 4a) and uncoated NMC (Figure 4c) confirms that the particle structure of NMC is maintained during the mixing process. In contrast, there is no Al signal detected in the EDX mapping of the uncoated NMC.

Figure 5 shows high-resolution SEM images of NMC coated by different amounts of Al<sub>2</sub>O<sub>3</sub> (Figure 5a–f) and uncoated NMC (Figure 5g,h). The pristine NMC consists of small primary NMC crystallites composing the secondary particle structure. The surface of the secondary structure is very rough, showing particles protruding from the plane and holes. The primary NMC crystallites itself have a very smooth and clean surface. The SEM images of the coated NMC particles clearly show the influence of the fraction of coating material on the coverage of the surface in the dry coating process. The image of NMC coated by 2 wt% Al<sub>2</sub>O<sub>3</sub> (Figure 5a,b) shows an almost complete coverage of the surface by a continuous and dense coating layer. With 1 wt% Al<sub>2</sub>O<sub>3</sub> (Figure 5c,d) still a quite continuous coating layer is achieved, but the protruding crystallites are only partially covered or covered by a very thin layer, while the areas in between are fully filled up by the metal oxide coating. A coating fraction of 0.5 wt% Al<sub>2</sub>O<sub>3</sub> (Figure 5e,f) predominantly fills the holes in the surface of the cathode material, while the rest is only sparsely covered. The influence of the different degrees of coverage of the cathode particle surfaces on the cycling performance is investigated in the electrochemical section below. Further in-depth analytical investigations were only conducted for the best performing coating fraction of 1 wt% Al<sub>2</sub>O<sub>3</sub> (see Section 2.3).

Scanning transmission electron microscopy in combination with energy dispersive X-ray spectroscopy (STEM-EDX) images of a cross section of NMC coated with 1 wt% Al<sub>2</sub>O<sub>3</sub> (Figure 6) elucidate in more detail how the coating material is distributed at the cathode particle surface. The thickness of the coating layer strongly depends on the morphology of the surface of the substrate material. Therefore, an exact value for the thickness of the coating layer cannot be determined. The roughness in the surface of NMC is compensated by the Al<sub>2</sub>O<sub>3</sub> coating layer. Our assumption from the SEM images, that the protruding crystallites are only partially covered or covered by a very thin layer, while the areas in between are fully filled up by the porous Al<sub>2</sub>O<sub>3</sub> coating, is confirmed by the STEM-EDX measurements. In areas of surface depressions, the coating thickness is increased whereas the protruding areas are only sparsely coated. A diffusion of aluminum into the bulk phase of the cathode material was not observed in high-resolution EDX images (see Figure S2, Supporting Information). We assume that the room-temperature coating process reduces diffusion of aluminum into the NMC phase to a minimum.

TEM images of cross sections of coated NMC show the microstructure of our coating layer (Figure 7a–c). The coating layer is not densely packed like in other types of coating approaches. The layer achieved with our dry mixing process using fumed alumina is porous, containing channels and holes, which probably enables a faster lithium-ion migration.<sup>[58]</sup> We assume that the channels are easily penetrated by the electrolyte. This would significantly reduce the impedance of the otherwise insulating Al<sub>2</sub>O<sub>3</sub> coating layer because the lithium-ion conductivity of the liquid electrolyte is orders of magnitude higher than that of the metal oxides.<sup>[66–69]</sup> The porosity of our coating layer is also confirmed by BET measurements. For uncoated NMC, a BET area of  $\approx 0.48 \text{ m}^2 \text{ g}^{-1}$  is measured, while the 1 wt% coated NMC has an increased BET surface of  $\approx 1.50 \text{ m}^2 \text{ g}^{-1}$ . The coating material itself is crystalline having the  $\gamma$ -Al<sub>2</sub>O<sub>3</sub> structure with a lattice parameter of 0.24 nm (Figure 7c).<sup>[64]</sup>

### 2.3. Electrochemical Measurements

To investigate the influence of the degree of coverage of the NMC surface by the coating material on cycling performance, 0.5, 1, and 2 wt% Al<sub>2</sub>O<sub>3</sub>-coated samples were evaluated in coin cells. The cycling performances of the coated materials are compared with the performance of uncoated NMC701515, as shown in Figure 8. The normalized cycling data are shown in Figure S3, Supporting Information. At the beginning, the rate

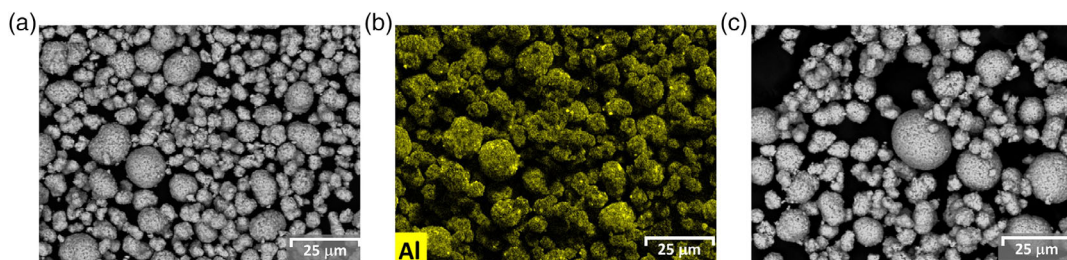


**Figure 4.** SEM images of NMC701515 coated with 1 wt% fumed Al<sub>2</sub>O<sub>3</sub>: a) backscattered electrons (BSE) image and b) EDX mapping of Al; c) BSE image of uncoated NMC for reference.

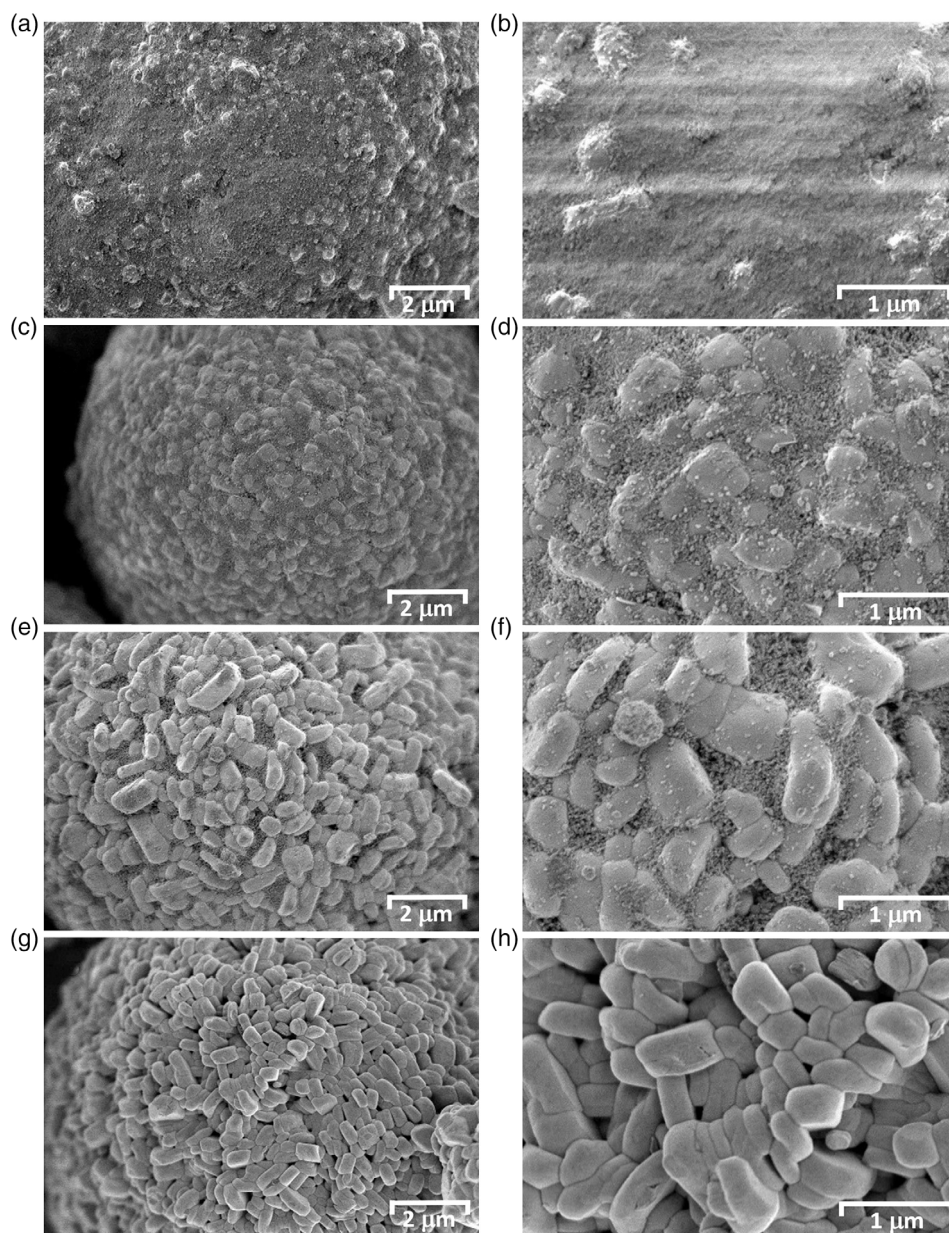


**Figure 5.** SEM images of NMC701515 coated by a,b) 2 wt%; c,d) 1 wt%; and e,f) 0.5 wt% fumed  $\text{Al}_2\text{O}_3$ , and g,h) uncoated NMC.

capabilities of the materials were evaluated. The cells were discharged at different rates from 0.1 to 4 C. The coated NMC materials show slightly higher initial specific discharge capacities than bare NMC at 0.1 C. This can be attributed to a beneficial side effect of a stable coating layer, which is improving the storage property of high-nickel materials by keeping off  $\text{CO}_2$  and  $\text{H}_2\text{O}$ .<sup>[25]</sup> The fresh NMC material was coated and both samples, coated and uncoated, were stored for several weeks before they were used for this study. Uncoated nickel-rich materials tend to suffer under lithium loss and form surface impurities, mostly carbonates, resulting in a capacity decrease and increase in impedance during cycling,<sup>[26]</sup> while the  $\text{Al}_2\text{O}_3$  coating layer prevents the formation of surface impurities by

effectively shielding the reactive NMC surface against  $\text{CO}_2$  and moisture.

With an increase in current density, the discharge capacities of the  $\text{Al}_2\text{O}_3$ -coated NMCs are superior to uncoated NMC. Only at the rate of 4 C, the 2 wt%  $\text{Al}_2\text{O}_3$ -coated NMC shows an inferior rate capability, implying that the rate performance is decreasing again, when the coating thickness of  $\text{Al}_2\text{O}_3$  and the C-rate gets too high. At the highest rate of 4 C, the best performance was achieved for the 1 wt%  $\text{Al}_2\text{O}_3$ -coated sample, showing a discharge capacity of  $134 \text{ mAh g}^{-1}$ . In comparison, uncoated NMC delivers only  $90 \text{ mAh g}^{-1}$  at this rate. These results indicate that our porous coating layer has a superior lithium-ion permeability compared with the SEI, which is formed by electrolyte

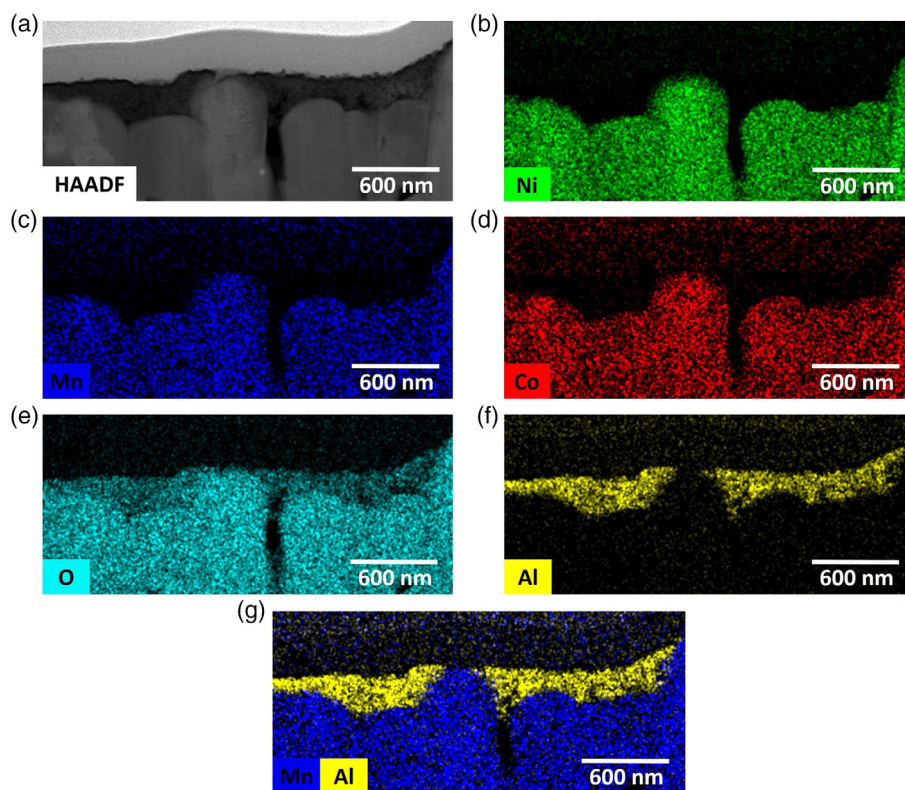


**Figure 6.** STEM-EDX analysis of a cross section of NMC701515 coated by 1 wt% fumed  $\text{Al}_2\text{O}_3$ . a) high-angle annual dark field scanning transmission electron microscopy (HAADF-STEM) Z-contrast image; b–f) mapping of Ni, Mn, Co, O, and Al; and g) two-color superposition image of Mn and Al showing the relative position of both signals.

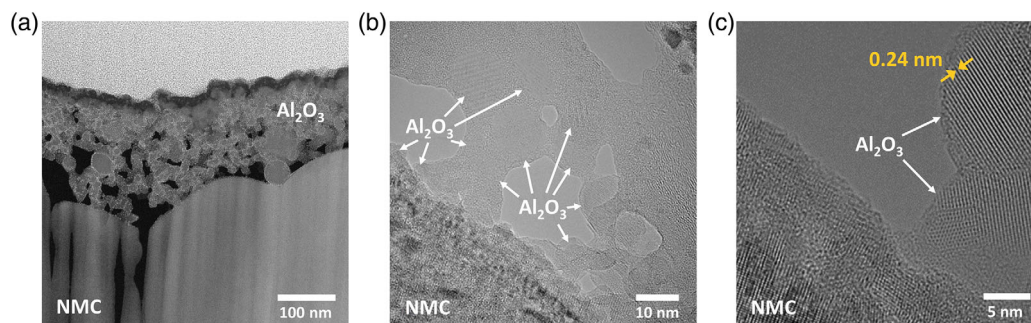


**Figure 7.** TEM images of cross sections of NMC coated by 1 wt% fumed  $\text{Al}_2\text{O}_3$  showing a,b) the porosity of the coating layer and c) the crystallinity of the coating material.

decomposition products on the uncoated NMC surface, as long as the coating thickness is not too high. We conclude that the coating layer successfully prevents the decomposition of electrolyte on the surface of the cathode material.

After the rate test a long-term cycling sequence is applied at 0.5 C. From the data (Figure 8) it can be clearly concluded that fumed  $\text{Al}_2\text{O}_3$  coatings improve the stability and cycle life of NMC. The best capacity retention was achieved for  $\text{Al}_2\text{O}_3$  coating fraction of 1 wt%, still having a discharge capacity of  $151 \text{ mAh g}^{-1}$  with a capacity retention of 92% (related to the first cycle with rate of 0.5 C, rate test included) after 100 cycles. For the

0.5 wt%  $\text{Al}_2\text{O}_3$ -coated sample a capacity of  $137 \text{ mAh g}^{-1}$  with a capacity retention of 86% and for the 2 wt%  $\text{Al}_2\text{O}_3$ -coated sample a capacity of  $131 \text{ mAh g}^{-1}$  with a retention of 83% are obtained. In comparison, the capacity decrease in uncoated NMC is distinct; only a capacity retention of 67% ( $99 \text{ mAh g}^{-1}$ ) after 100 cycles is obtained.

The optimal coating fraction to achieve the best overall cycling performance for the investigated NMC701515 is 1 wt% of fumed  $\text{Al}_2\text{O}_3$ , combining good rate capability with high capacity retention. However, the cycling performance strongly depends on the degree of coverage of the surface and the thickness of the coating

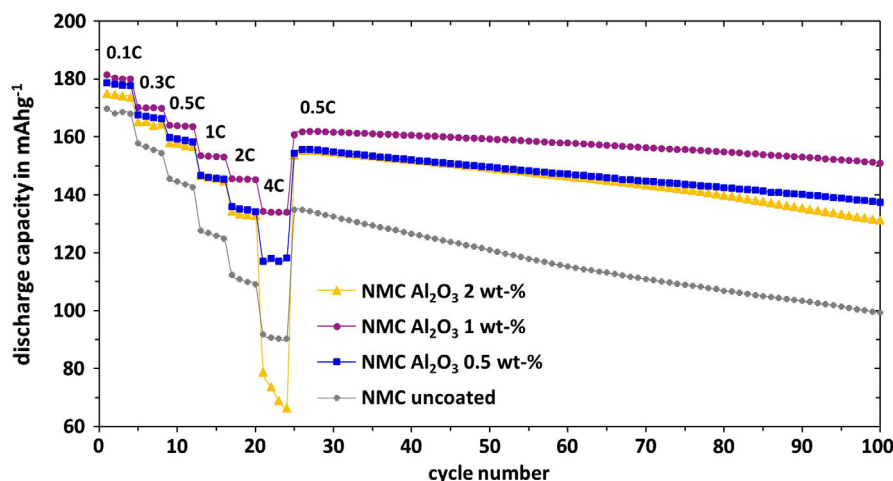


**Figure 8.** Cycling performance of NMC701515 dry-coated with different amounts of fumed  $\text{Al}_2\text{O}_3$  and uncoated NMC701515 (average of three cells each, lithium metal as anode).

layer, which, in turn, depends on the surface morphology on the cathode material. Consequently, the optimum amount of coating material could vary for different cathode materials.

To confirm the negative effect on the cycling performance of annealing high-nickel NMC coated with fumed  $\text{Al}_2\text{O}_3$ , the NMC coated with 1 wt%  $\text{Al}_2\text{O}_3$  was annealed at  $600^\circ\text{C}$  for 8 h and then evaluated electrochemically. The cycling data are shown in Figure S4, Supporting Information. The rate and long-term cycling capacities of the annealed sample are still superior to the uncoated NMC, but significantly lower than for the nonannealed equivalent. The inferior cycling behavior of the annealed sample is mostly attributed to a reduced porosity of the coating layer caused by melting and compaction at high temperatures, impeding the penetration by liquid electrolyte. For the annealed sample, a BET surface of only  $0.58\text{ m}^2\text{ g}^{-1}$  is detected, while the nonannealed sample shows a BET surface of  $\approx 1.50\text{ m}^2\text{ g}^{-1}$ . The diffusion of aluminum ions into the bulk phase of NMC after annealing, as observed by Han et al.,<sup>[65]</sup> could contribute to the inferior cycling performance. However, a detailed analysis of aluminum penetration into NMC is beyond the scope of this study.

The improved cycling behavior of the coated NMC is attributed to a successful protection of the reactive surface of high-nickel cathode material from side reactions by the fumed  $\text{Al}_2\text{O}_3$  coating layer as further proven in the following electrochemical impedance spectroscopy (EIS) section. The surface is shielded against electrolyte decomposition and the formation of a thick SEI layer, which hinders the diffusion of lithium ions and electrons, leading to capacity fade, is suppressed.<sup>[70,71]</sup> Furthermore, the attack of acidic HF, produced by  $\text{LiPF}_6$  in the electrolyte, is also prevented due to the HF scavenging effect of  $\text{Al}_2\text{O}_3$ .<sup>[49–51]</sup> This inhibits the dissolution of transition metal ions out of the surface of the cathode material into the electrolyte and the resulting lattice distortion in the cathode material, which is also an important reason for decreasing capacity during charge–discharge processes.<sup>[3,15,19,20]</sup>

EIS measurements were performed for deeper investigations on the enhanced cycling performance of fumed  $\text{Al}_2\text{O}_3$ -coated NMC. **Figure 9** shows Nyquist plots of impedance

measurements of cells containing uncoated NMC and NMC coated by 1 wt% fumed  $\text{Al}_2\text{O}_3$  before cycling and after several cycles in charged state. The experimental results of the uncycled cells show one depressed semicircle in the high-to-mid frequency range and a straight line at low frequencies, suggesting that these systems can be interpreted using an equivalent circuit composed of a resistor, a resistor/constant phase element (CPE) relaxation loop, and a Warburg element at low frequencies. The equivalent circuit used for EIS simulation to get quantitative values for the resistances is shown in Figure 9e.  $R_s$  (series resistance) is the sum of electronic resistances from the electrodes, leads, and ionic resistance of the electrolyte of the cell at high frequencies;  $R_{CT}$  is the charge transfer resistance, and  $C_{dl}$  is the constant-phase element corresponding to the electric double-layer capacitance. The tail at low frequency is assigned to a Warburg impedance ( $Z_w$ ), exhibiting the diffusion of lithium in the electrode.

EIS spectra of cycled cells contain an additional depressed semicircle at high-to-mid frequency, suggesting that these systems can be interpreted using an equivalent circuit with an additional resistor/CPE relaxation loop. A typical equivalent circuit for such systems is used for EIS simulation, as shown in Figure 9f.  $R_{SEI}$  represents the interfacial film resistance and  $C_{SEI}$  is the constant-phase element corresponding to the SEI capacitance. The resistance values according to the fitting results from the equivalent circuits are shown in **Table 1**. Note that these measurements were performed with full cells and the presented values for the resistances from the fits are not exclusively specific for the cathode, as the anode side is contributing. Nevertheless, all differences in the EIS data can be related alone to the coating layer because this is the only difference between the cells.

There is a significantly increased  $R_{CT}$  value for the coated NMC ( $323.0\ \Omega$ ) compared with uncoated NMC ( $74.7\ \Omega$ ) before cycling. This effect is attributed to the insulating  $\text{Al}_2\text{O}_3$  coating layer. After the electrochemical formation of the cell, the charge transfer resistance for both NMC uncoated and coated decreases significantly. This can be explained by the formation of a conductive layer on the surface of cathode materials. The decrease in  $R_{CT}$  is relatively much stronger for the coated NMC

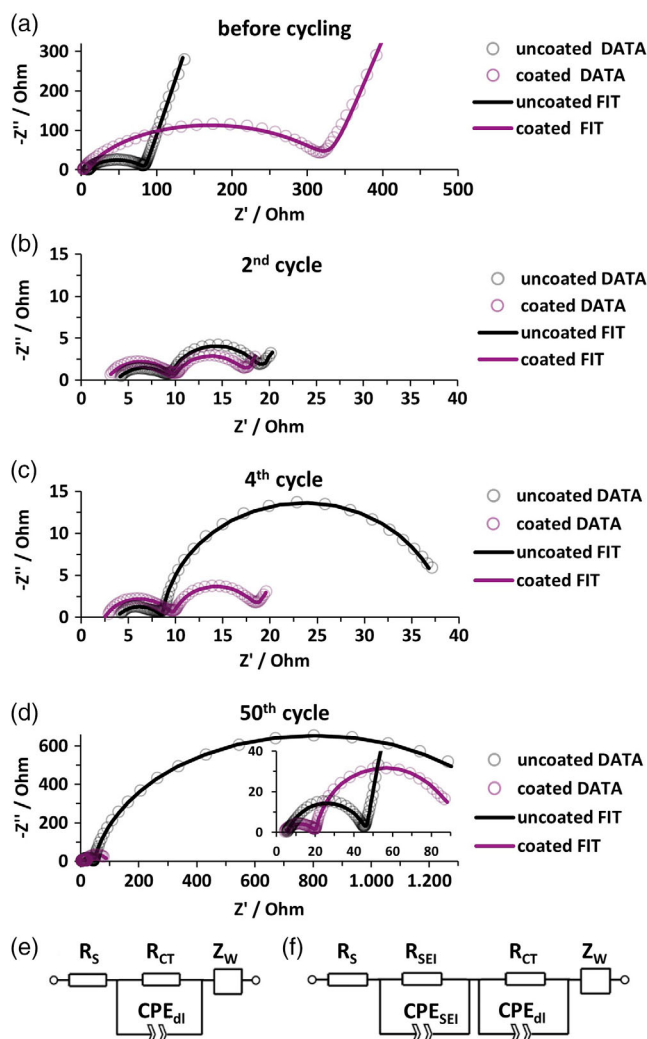


**Figure 9.** Nyquist plots of the impedance spectra of cells containing uncoated NMC701515 and NMC coated by 1wt% fumed Al<sub>2</sub>O<sub>3</sub> a) before cycling, b) after 2nd charge, c) 4th charge, and d) 50th charge (inset picture displays the plot at an enlarged scale). e) The corresponding equivalent circuit model for fitting the data before cycling and f) the model for fitting the data of charged states after different cycles, to get quantitative values of resistance.

(from 323.0 to 7.4 Ω) compared with the uncoated (from 74.7 to 9.1 Ω). Also, the resulting value of R<sub>CT</sub> is lower for the coated NMC. This indicates a transformation reaction of the pristine

**Table 1.** Fitted impedance parameters by the corresponding equivalent circuits (Figure 9e,f) of uncoated and NMC coated by 1 wt% fumed Al<sub>2</sub>O<sub>3</sub> and the corresponding approximated lithium-ion diffusion coefficients (D<sub>Li</sub>).

	NMC uncoated			NMC coated by 1 wt% fumed Al <sub>2</sub> O <sub>3</sub>		
	R <sub>SEI</sub> [Ω]	R <sub>CT</sub> [Ω]	D <sub>Li</sub> [cm <sup>2</sup> s <sup>-1</sup> ]	R <sub>SEI</sub> [Ω]	R <sub>CT</sub> [Ω]	D <sub>Li</sub> [cm <sup>2</sup> s <sup>-1</sup> ]
Before cycling	–	74.7	–	–	323.0	–
2nd Cycle	5.8	9.1	2.62689 × 10 <sup>-10</sup>	7.2	7.4	3.88461 × 10 <sup>-10</sup>
4th Cycle	4.9	30.0	2.72643 × 10 <sup>-11</sup>	7.3	8.7	3.19176 × 10 <sup>-10</sup>
50th Cycle	40.4	1490.4	2.07405 × 10 <sup>-14</sup>	16.0	65.7	8.3302 × 10 <sup>-13</sup>

coating to a less resistant coating layer in the electrochemical formation step. During prolonged cycling the charge transfer resistance is growing clearly much faster for the uncoated NMC in comparison with the coated NMC. After the 50th charging step, the R<sub>CT</sub> value for the uncoated NMC has risen to 1490.4 Ω, while the NMC coated by Al<sub>2</sub>O<sub>3</sub> only shows a R<sub>CT</sub> value of 65.7 Ω.

In the first cycles, the resistance values of the SEI layer for the uncoated NMC are still below those for the NMC coated. R<sub>SEI</sub> for the uncoated cell decreases from 5.8 to 4.9 Ω in second to fourth charge. This could be ascribed to the activation of the material in the initial several cycles and the gradual formation of the ion conductive SEI layer.<sup>[72,73]</sup> In contrast, the R<sub>SEI</sub> value for the coated NMC is increasing only slightly from 7.2 to 7.3 Ω. After the initial cycles, the R<sub>SEI</sub> values are increasing also for the uncoated material and they increase faster than those for coated material. After the 50th charge, R<sub>SEI</sub> for uncoated NMC (40.4 Ω) is significantly higher than the value for the coated NMC (16.0 Ω). Both the improved R<sub>SEI</sub> and R<sub>CT</sub> values achieved for coated NMC point to a successful protection of the reactive surface of the cathode material by the fumed Al<sub>2</sub>O<sub>3</sub> layer while providing enhanced lithium-ion diffusion.

The coating stabilizes the cathode/electrolyte interface. Detrimental side reactions such as metal ion dissolution during the charge–discharge process, decomposition of electrolyte, and deposition of by-products are reduced; the thickness of SEI film is thus restrained.<sup>[31,73]</sup> As a consequence an improved long-term cycling stability is achieved for the coated NMC. The reduced growth of impedance values by the coating layer further reveals an enhancement in the kinetics of lithium-ion diffusion through the surface layer and the charge transfer reaction and a consequent increase in rate capability, which is in agreement with the enhanced rate capability of coated NMC as mentioned earlier.<sup>[70,74]</sup> In contrast, at the uncoated NMC surface, electrolyte decomposition is ongoing and the SEI layer is growing and thickening, which is impeding the transport of lithium ions.<sup>[73,75]</sup>

To confirm the positive influence of the fumed Al<sub>2</sub>O<sub>3</sub> coating layer on the lithium-ion diffusion, the (apparent) lithium-ion diffusion coefficients were calculated from the linear part of the low frequency region (Warburg impedance Z<sub>w</sub>) of the EIS data. The lithium diffusion coefficients were approximated by the following equation<sup>[38,73,76–79]</sup>

$$D_{Li} = \frac{R^2 T^2}{2A^2 n^4 F^4 C^2 \sigma^2} \quad (1)$$

where R is the gas constant, T is the absolute temperature, A is the surface area of the electrode, which was estimated based on the BET area (0.48 m<sup>2</sup> g<sup>-1</sup> for NMC701515), n is the number of

electrons involved in the intercalation step ( $n = 1$ ),  $F$  is the Faraday constant,  $C$  is the molar concentration of lithium ions in the electrode, and  $\sigma$  is the Warburg factor.

The Warburg factor is obtained from the slope of  $Z'$  versus  $\omega^{-1/2}$  plots ( $\omega$  is the angular frequency) in the Warburg region.<sup>[38,73,76–79]</sup> The  $Z'$  versus  $\omega^{-1/2}$  plots, along with the linear fitting curves, for cycles 2, 4, and 50 are shown in Figure S5, Supporting Information. The calculated lithium-ion diffusion coefficients are shown in Table 1. The apparent diffusion coefficients for the pristine and the coated NMC are decreasing with increasing cycle number due to aging of the electrode materials. Hereby the diffusion coefficients for the  $\text{Al}_2\text{O}_3$ -coated sample decrease much slower than for the uncoated NMC, confirming that the fumed  $\text{Al}_2\text{O}_3$  coating layer helps to maintain the lithium-ion diffusion in the electrodes more stable at prolonged cycling. In addition, the values for the  $\text{Al}_2\text{O}_3$ -coated cathodes are superior to those of uncoated in all cycles. The larger apparent lithium-ion diffusion coefficients in the  $\text{Al}_2\text{O}_3$ -coated cathodes explain, in addition to the reduced  $R_{\text{SEI}}$  and  $R_{\text{CT}}$  impedance values, the increased rate capability of the coated electrode material.

#### 2.4. Characterization of Cycled Electrodes

Cross sections from cycled cathodes were prepared and investigated by SEM-EDX. The BSE image of the cathode containing the fumed alumina-coated NMC particles (Figure 10a) shows intact particles. In the SEM-EDX (Figure 10b) and the STEM-EDX mapping (Figure 11f) of the cycled NMC material, it can be seen that the  $\text{Al}_2\text{O}_3$  coating layer is still on the surface of each cathode material particle and intact. This demonstrates that our coating layer is not only stable during slurry preparation process while cathode manufacturing, but also stays stable and persistent during battery cycling.

Obviously, the BSE image of the uncoated NMC electrode (Figure 10c), cycled under exactly the same conditions, demonstrates strong crack formation and particle disintegration after cycling. Some of the NMC particles have completely fragmented into primary crystallites. This causes loss of inner particle connectivity and gives rise to increased polarization.<sup>[2]</sup> The significant increase in surface area of the cathode material, which is exposed to the electrolyte, results in a further electrolyte decomposition and SEI formation, as well as surface transformations, on the new generated surfaces.<sup>[14]</sup> This phenomenon leads to a further impedance increase, as shown in Figure 9, and contributes to degradation of performance and capacity fade. Figure 10c

also supports the findings of Yang et al.<sup>[80]</sup> that the active cathode particles, within the electrode, contribute to the cell-level chemistry differently in time and position. The crack formation and particle disintegration are more progressed in particles near the separator (on the right side of Figure 10c), possibly due to a higher degree of reaction, caused by their favorable kinetics.

These findings demonstrate that coating layers made by fumed alumina are able to protect surfaces of cathode materials from detrimental side reactions. Phase transformations such as the formation of a NiO-like phase due to the reduction of  $\text{Ni}^{4+}$  in a highly delithiated state and oxygen loss as well as transition metal rearrangement have been associated to initiate cracks at the cathode particle surface and the subsequent particle disintegration.<sup>[6,8–10,13,24]</sup>

While severe surface destruction has been reported in the literature on cycled pristine NMC, showing a transition from layered over a disordered layered to a rock salt structure on the surface,<sup>[8,14,80–83]</sup> we observed in HRTEM analysis that the layered structure of the NMC is almost completely maintained during cycling of the cycled  $\text{Al}_2\text{O}_3$ -coated NMC. As shown in Figure S6, Supporting Information, only a very thin ( $\leq 1$  nm) disordered layered area is found directly at the edge of the interface between the NMC and the  $\text{Al}_2\text{O}_3$  coating layer. This demonstrates the protecting effect of the fumed  $\text{Al}_2\text{O}_3$  coating very well, i.e., transformations of the reactive surface of high-nickel NMC are effectively inhibited.

STEM-EDX images reveal that during cycling a new fluorine containing layer has been formed on the surface (Figure 11g,h). We note that the NMC material itself does not contain fluorine. The fluorine EDX signals in the NMC material in Figure 11g result from an overlap of the manganese and cobalt signals with the fluorine peak. An overlay image of aluminum, fluorine and manganese (Figure 11h) shows that the fluorine containing layer is predominantly placed on top of the surface, indicating that a new phase precipitates during cycling. A more in-depth analysis of the cycled material was performed using scanning transmission electron microscopy-electron energy loss spectroscopy (STEM-EELS).

Figure 12 shows EELS maps of the cycled coated NMC material. The coating layer containing Al is clearly visible on top of the NMC material (Figure 12a). The fluorine containing layer observed in EDX at the surface of the coating is detected (Figure 12b). Mapping of the Li K-edge (Figure 12c) shows the presence of lithium in the NMC material as well as in the fluorine containing layer. Comparison of the electron energy loss

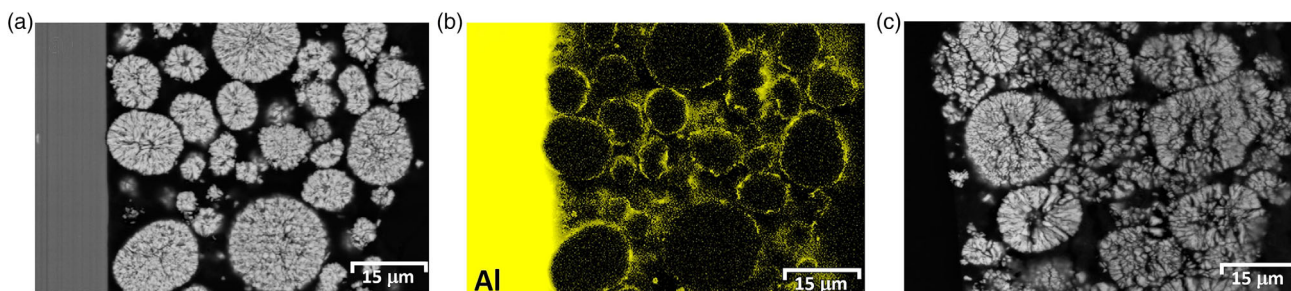


**Figure 10.** SEM-EDX images of cross sections of cycled cathodes of NMC701515 coated by 1 wt% fumed  $\text{Al}_2\text{O}_3$ : a) BSE image, b) EDX mapping of Al, c) BSE image of uncoated NMC as a comparison (current collector was detached during sample preparation process).

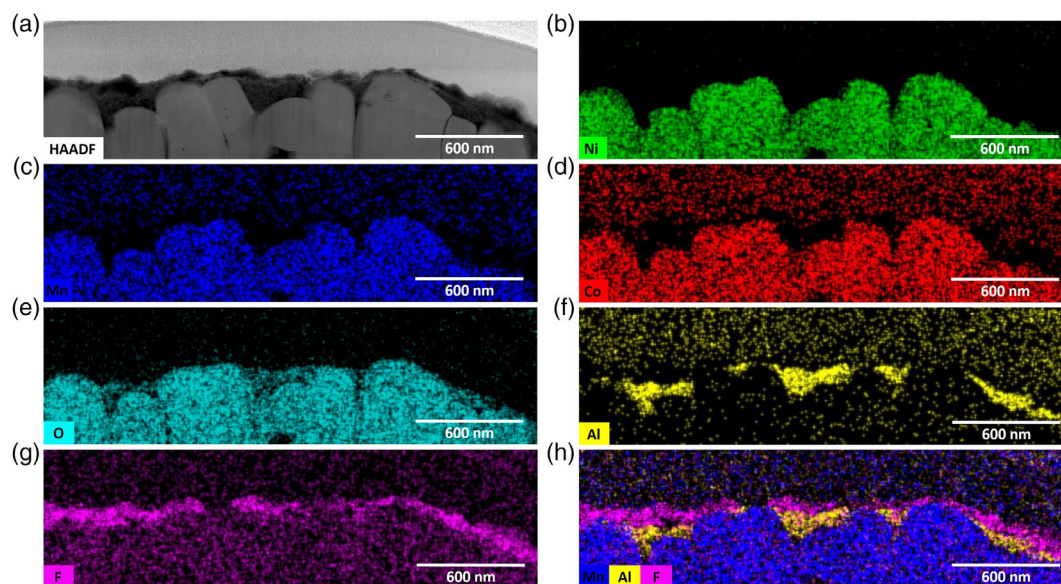


**Figure 11.** STEM-EDX analysis of a cross section of cycled NMC701515 coated by 1 wt% fumed  $\text{Al}_2\text{O}_3$ . a) HAADF-STEM Z-contrast image; b–g) mapping of Ni, Mn, Co, O, Al, and F; and h) superposition image of Mn, Al, and F.

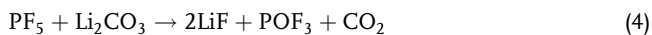
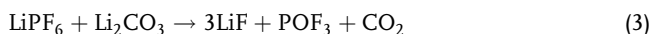
near edge structure (ELNES) spectra of the Li and F K-edges of the fluorine containing layer with the spectra of a LiF reference sample reveals that the formed layer on top of the coating is LiF (Figure 12i,j). In Figure 12e,f, multilinear least squares (MLLS) fitting of the Li K-edge of two experimental spectra of the Li K-edge of the fluorine containing layer (Figure 12e) and the NMC701515 (Figure 12f) confirms the presence of LiF only in the surface layer.

LiF is a well-known component in SEI layers of electrodes when  $\text{LiPF}_6$  is used as the conduction salt in the electrolyte. Several reactions have been proposed to explain the formation of LiF (Equation (2)–(6)).<sup>[84–89]</sup>

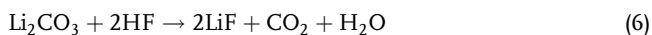
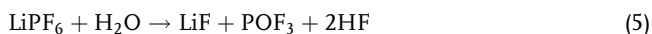
The decomposition of  $\text{LiPF}_6$



The reaction of  $\text{LiPF}_6$  or  $\text{PF}_5$  with  $\text{Li}_2\text{CO}_3$ , which is possible because high-nickel materials tend to form carbonates on the surface during storage<sup>[25–27]</sup>



The reactions with traces of water in the electrolyte, which are present in all commercial formulations<sup>[12,18]</sup>

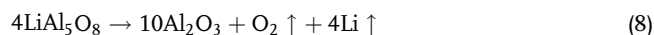


The O K-edge map of the cycled sample (Figure 12d) shows that an oxygen signal is present in the NMC and the coating layer. While in the coating layer of the uncycled sample the fine structure of the oxygen K-edge can be clearly identified as  $\gamma\text{-Al}_2\text{O}_3$  (Figure 12k, green curve), in the O K-edge of the coating layer

of the cycled sample, a small shoulder is detected centered around 537 eV (Figure 12k, black and red curves) and an additional prepeak at 531 eV appears. The size of the prepeak in the spectra strongly depends on the chosen region in the coating layer. The intensity map of this prepeak, integrated between 528 and 532 eV, is shown in Figure 12g. It is important to note that contrast in NMC (in Figure 12g) is due to the presence of spectral weight at the O K-edge of NMC701515 in this range of energy, as seen in the reference spectrum (Figure 12k, orange curve).

Hetaba et al.<sup>[90]</sup> observed the same phenomenon measuring  $\gamma\text{-LiAlO}_2$ . They discovered that  $\text{LiAlO}_2$  undergoes the following transformation caused by the electron beam:  $\text{LiAlO}_2 \rightarrow \text{LiAl}_5\text{O}_8 \rightarrow \text{Al}_2\text{O}_3$ . Their detected O K-edge spectra show the same shoulder and additional peak at 531 eV. At the beginning of the transformation, the prepeak intensity increases as can be observed in our  $\text{LiAlO}_2$  reference after 15 s (purple curve in Figure 12k, compared with the fresh  $\text{LiAlO}_2$  commercial powder—pink curve). After the transformation process is completed, the prepeak disappears again. Thus, the peak is observed as long as the transformation from  $\text{LiAlO}_2$  to  $\text{Al}_2\text{O}_3$  is taking place. This peak is attributed to a  $\pi^*$ -transition of molecular oxygen ( $\text{O}_2$ ) that is lost during the transformation process.

The postulated reaction is<sup>[90]</sup>



Because we did not detect any other formed species in our coating layer after cycling and we observed the same phenomenon as Hetaba et al. for the oxygen signal, we suspect an incorporation of lithium ions in our  $\gamma\text{-Al}_2\text{O}_3$  coating layer during cycling and consequently a partial formation of  $\text{LiAlO}_2$  (or more general  $x\text{Li}_2\text{O}\cdot\text{Al}_2\text{O}_3$ ). The detected prepeak cannot occur from  $\text{Al}_2\text{O}_3$ , as it is stable to the electron irradiation.<sup>[90]</sup>

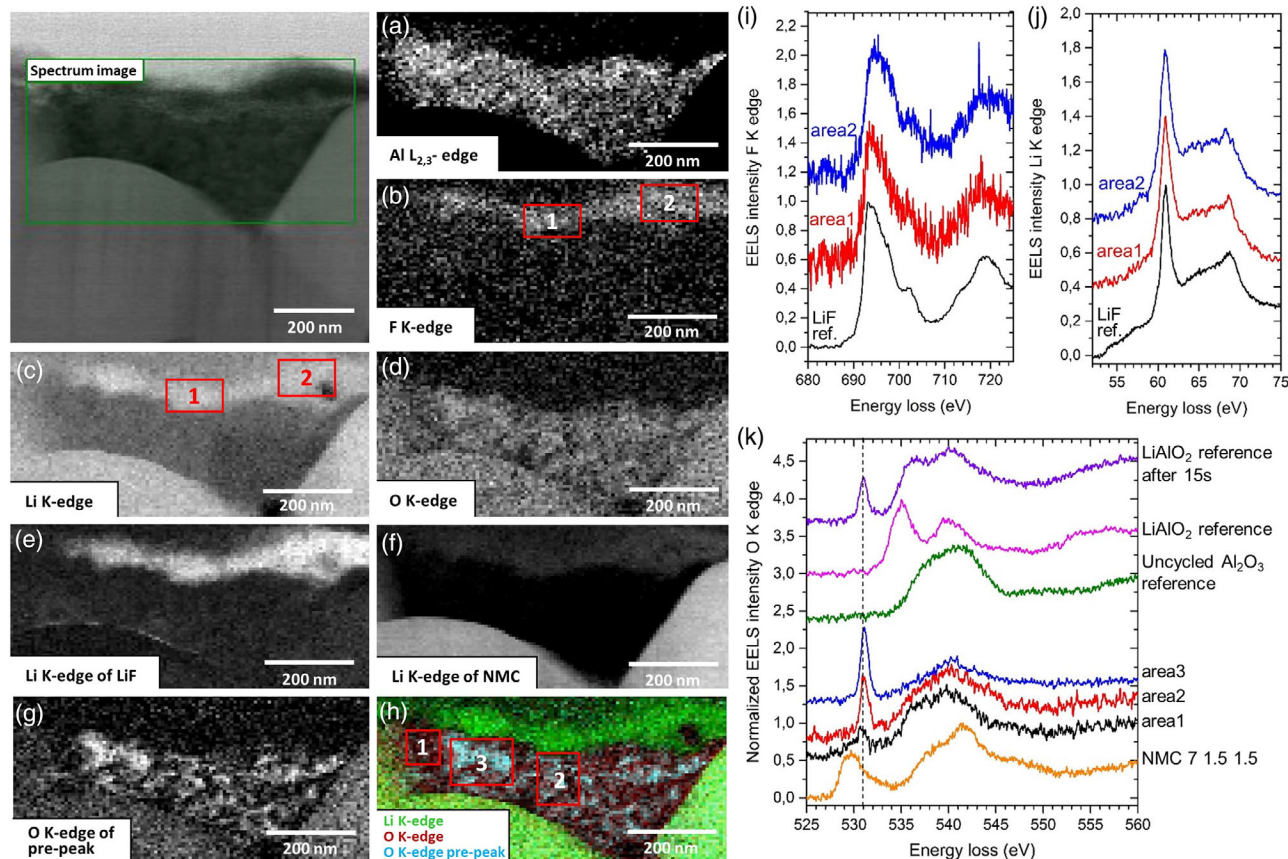


**Figure 12.** STEM-EELS analysis and spectra of selected areas of a cross section of cyclized NMC701515 coated with 1 wt% fumed  $\text{Al}_2\text{O}_3$ . Compositional spectrum images corresponding to the Al  $L_{2,3}$ -edge, F, Li, and O K-edges are, respectively, shown on panels a)–d). e), f) The MLLS fitting of the Li K-edge region using fine structures corresponding to LiF and NMC701515. g) The distribution of the prepeak to the O K-edge integrated between 528 and 532 eV (it is important to note that contrast in the NMC701515 is due to the presence of spectral weight at the O K-edge of NMC701515 in this same energy range as visible in panel (k)). h) A false color image of the Li K-edge (green), O K-edge (red), and prepeak of the O K-edge (blue). i, j) The experimental ELNES spectra of the F and Li K-edges, respectively, in areas 1 and 2 of panels (b) and (c) compared with a reference spectra taken on a commercial LiF powder, confirming the presence of a LiF layer at the surface of the coating. k) Spectra of the O K-edge taken in areas 1, 2, and 3 of panel (h) compared with uncycled  $\text{Al}_2\text{O}_3$  and  $\text{LiAlO}_2$  reference spectra.

Furthermore, no residual Li K-edge spectral weight was detected in the cyclized coating layer using EELS within the detection limit of the technique. It is interesting to note that the fine structures of the Al  $L_{2,3}$ -edge spectra (see Figure S7, Supporting Information) in areas 1–3 (Figure 12h), where we see significant differences on the O K-edges, do not show any differences, and are almost identical to the noncyclized reference coating ( $\gamma\text{-Al}_2\text{O}_3$ ), indicating that the prepeak is related to molecular oxygen having no bonding to the aluminum. It is very different to the spectrum of  $\text{LiAlO}_2$  confirming the hypothesis made earlier. To further investigate our assumption and to rule out the role of electron beam damage, the cyclized sample was analyzed by X-ray photoelectron spectroscopy (XPS) measurements.

XPS measurements (Figure 13) confirm the formation of  $\text{Li}_x\text{Al}_2\text{O}_3/\text{LiAlO}_2$ . In the Li 1s spectrum, a signal at 54.6 eV is detected, which is identical to the signal of a  $\text{LiAlO}_2$  reference sample. The formation of a LiF layer on top could also be confirmed by XPS data. The peaks at 55.7 eV in the Li 1s spectrum and at 685.0 eV in the F 1s spectrum correspond to the signals of

the LiF reference sample. After sputtering into the electrode (approximately 130 nm via tantalum oxide reference), the amount of detected LiF is significantly decreased, while the amount of  $\text{Li}_x\text{Al}_2\text{O}_3/\text{LiAlO}_2$  remains nearly constant. The signals at 56.7 eV in the Li 1s spectrum and at 686.0 eV in the F 1s spectrum are attributed to decomposition products of  $\text{LiPF}_6$  such as  $\text{Li}_x\text{PF}_y/\text{Li}_x\text{PO}_y\text{F}_z$ <sup>[85,91–94]</sup> and the signal at 687.7 eV to polyvinylidene fluoride (PVDF) binder.<sup>[91,95]</sup>

The partial formation of  $\text{Li}_x\text{Al}_2\text{O}_3/\text{LiAlO}_2$  could not be further confirmed by the Al signal in the XPS analysis due to the strong overlap of the Al signal with the Ni signal. However, there are reports in the literature for the formation of  $\text{LiAlO}_2$  on  $\text{Al}_2\text{O}_3$ -coated materials, which do not contain nickel. For example, Sun et al. observed  $\text{LiAlO}_2$  formation during cycling via XPS in a thin ALD layer of  $\text{Al}_2\text{O}_3$  on sulfur cathodes,<sup>[96]</sup> while Ahn et al. show the formation of  $\text{LiAlO}_2$  on  $\text{Al}_2\text{O}_3$ -coated Si electrodes.<sup>[97]</sup>

As EELS and XPS measurements indicate the partial formation of  $\text{Li}_x\text{Al}_2\text{O}_3/\text{LiAlO}_2$ , we strongly suspect an incorporation of lithium ions in our  $\gamma\text{-Al}_2\text{O}_3$  coating layer during cycling. Also, the

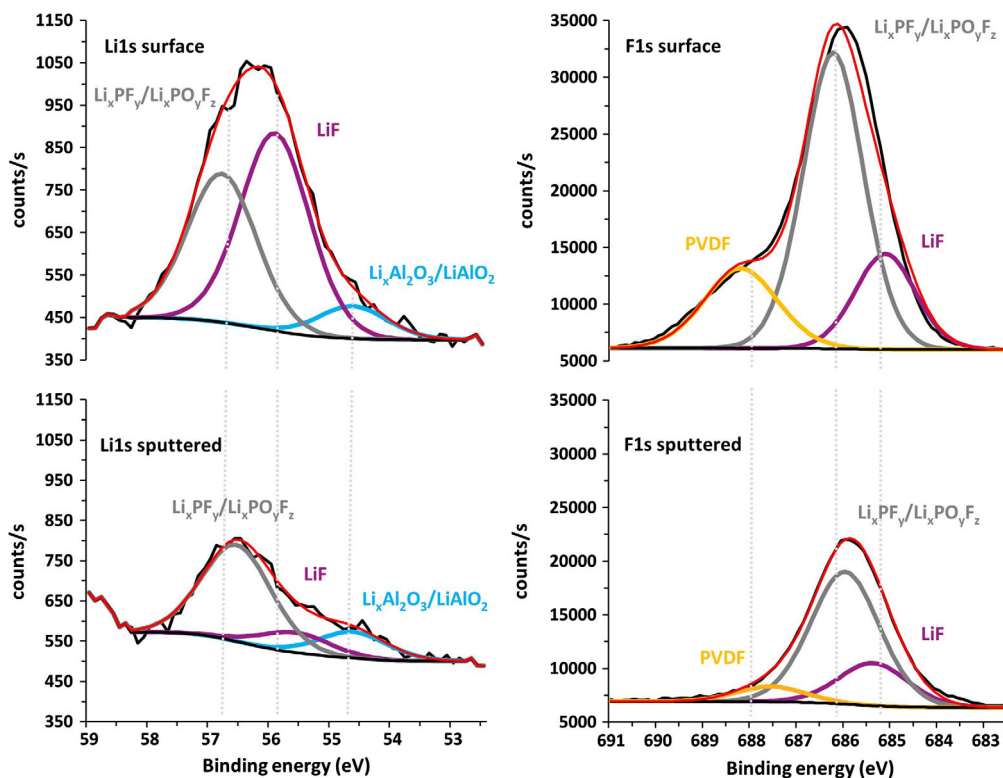


**Figure 13.** XPS analysis of a cycled electrode containing NMC coated with 1 wt% fumed  $\text{Al}_2\text{O}_3$ . Li 1s and F 1s spectra of the surface (top) and after sputtering (bottom) into the electrode (approximately 130 nm via tantalum oxide reference).

significantly decreased impedance value for  $R_{CT}$  detected in the EIS measurements of the coated NMC after the electrochemical formation of the cell, compared with the sample before cycling, shows that the  $\text{Al}_2\text{O}_3$  coating layer is transforming to a less insulating coating. This phenomenon could also be explained by the incorporation of lithium ions in the coating layer.<sup>[98]</sup>

Our findings support previous DFT calculations, proposing that  $\text{Al}_2\text{O}_3$  coatings are lithiated during cycling.<sup>[68,99]</sup> They suggest that in LIBs the  $\text{Al}_2\text{O}_3$  coating layers first absorb lithium ions and are lithiated until a thermodynamically stable phase is reached. Then, extra lithium ions overflow by passing through the coating layer.

Therefore, we assume that lithium ions diffuse through the porous coating layer via preferred paths with the highest local diffusion coefficient. Note that the coating layers built of fumed  $\text{Al}_2\text{O}_3$  aggregates do not form a highly porous network. Due to the coalescence and compaction of the aggregates, there are also many areas present in the coating layer with only few or no pores at all. In these regions, the lithium ions have to migrate through the coating material; and especially at moderate-to-high discharge rates, it is very likely that migration through thin barriers of coating material will be favored instead of diffusion through a widely ramified labyrinth of channels filled by liquid electrolyte. In these locations, lithium ions start to interact with the  $\text{Al}_2\text{O}_3$  coating and form  $\text{Li}_x\text{Al}_2\text{O}_3/\text{LiAlO}_2$ . This explains why we only see a formation of  $\text{Li}_x\text{Al}_2\text{O}_3/\text{LiAlO}_2$  in certain parts of the coating layer (Figure 12g). Along these defined paths the lithium diffusivity is enhanced permanently and all following lithium ions can

pass the coating layer faster, due to an increased lithium-ion conduction/diffusion coefficient in  $\text{Li}_x\text{Al}_2\text{O}_3/\text{LiAlO}_2$  compared to  $\text{Al}_2\text{O}_3$ .<sup>[99–101]</sup>

The formation of  $\text{Li}_x\text{Al}_2\text{O}_3/\text{LiAlO}_2$  in the coating layer contributes to the increased rate performance and lithium-ion diffusivity in the electrode, explaining the significant increase in rate performance, which was observed in the electrochemical evaluation part.

### 3. Conclusion

We present a facile and fast dry powder coating method of high-nickel NMC701515 by nanostructured fumed  $\gamma\text{-Al}_2\text{O}_3$ . In the high intensity mixing process, the coverage of the CAM surface strongly depends on the applied amount of coating material. The resulting layer shows a certain porosity and sticks on the surface, even after slurry preparation and extensive cycling. There is no need for an additional calcination step after dry coating for fixing the coating material. This prevents the diffusion of Al into the bulk phase of the NMC, which was found to lead to poor overall cycling performance. However, the cycling performance strongly depends on the degree of coverage of the surface and the thickness of the coating layer, which, in turn, depends on the surface morphology of the cathode host material. The optimal coating amount to achieve the best overall cycling performance for the here investigated NMC701515 is 1 wt% of  $\text{Al}_2\text{O}_3$ , combining good rate capability with high capacity retention. A high coverage

of the CAM surface by an almost continuous coating layer, showing a certain porosity with excellent lithium-ion diffusivity, was achieved.

Electrochemical cycling and impedance measurements convincingly show that the fumed  $\text{Al}_2\text{O}_3$  coating layer successfully protects the surface of high-nickel NMC from detrimental side reactions while maintaining a porous structure allowing lithium ions to diffuse through. The coating layer leads to significantly improved  $R_{\text{SEI}}$  and  $R_{\text{CT}}$  values during cycling and consequently to reduced total resistance in the battery, and to improved lithium-ion diffusion coefficients in the electrodes, ensuring an enhanced rate performance, capacity retention, and cycle life.<sup>[38]</sup> SEM analysis of cycled electrodes reveals that crack formation and particle disintegration of the NMC are prevented effectively by fumed  $\text{Al}_2\text{O}_3$  coating layers. EELS and XPS measurements indicate that lithium ions start to interact with the  $\text{Al}_2\text{O}_3$  coating and form  $\text{Li}_x\text{Al}_2\text{O}_3/\text{LiAlO}_2$  in certain locations. We assume that lithium ions diffuse through the coating layer along preferred paths with the highest diffusion coefficients. This can occur partly by diffusion through channels filled with liquid electrolyte and partly by migration through the coating material. In these areas the lithium ions react with the coating material, enhancing the lithium-ion conduction permanently at these defined paths and subsequently also the rate performance.

In conclusion, the developed dry coating process is a fast and practical, cost and energy efficient as well as an environmentally friendly method to successfully protect and enhance the performance of CAMs. The process is easily scalable to large-scale high intensity mixers (e.g. from Eirich) and therefore very suitable for industrial manufacturing. Furthermore, the coating process is not limited to NMC cathode material; it can be applied on almost all different types of CAMs. Also, the coating material is not limited to  $\text{Al}_2\text{O}_3$ .

## 4. Experimental Section

*Details about the Sample Preparation:* For this study, commercial NMC701515 powder (obtained from Linyi Gelon LIB Co.) and nanostructured fumed  $\text{Al}_2\text{O}_3$  ("AEROXIDE Alu 130" from Evonik Operations GmbH) were used. A lab scale high energy mixer from Somakon Verfahrenstechnik UG (Somakon mixer MP-GL) was used for carrying out the dry coating process. The mixing unit of the Somakon mixer consists of two very high-speed rotating rotors with four blades each (see Figure S8, Supporting Information) and has a volume of 0.5 L. However, this process can easily be transferred to large-scale industrial mixers (e.g. from Eirich GmbH up to a mixer size of 3000 L). For dry coating, the NMC powder was mixed with the respective amount (0.5, 1.0, and 2.0 wt%) of nanostructured  $\text{Al}_2\text{O}_3$  powder in the high energy mixer at first for 1 min at 500 rpm to homogeneously mix the two powders. Afterward the mixing intensity was increased to 2000 rpm for 6 min to deagglomerate the nanostructured  $\text{Al}_2\text{O}_3$  into smaller aggregates that adhere at the surface of NMC. The coated CAM is used as received after mixing process.

To confirm the negative effect on the cycling performance of annealing high-nickel NMC coated with fumed  $\text{Al}_2\text{O}_3$ , the coated NMC was annealed at 600 °C for 8 h in air.

*PSD:* PSD analysis was conducted using a Beckman Coulter LS 13320 laser diffraction particle size analyzer, equipped with a universal liquid module and a polarization intensity differential scatter (PIDS unit). This combination of techniques allowed establishing grain size distribution curves composed of 116 logarithmic grain size classes, covering a range of 0.04–2000  $\mu\text{m}$ . The main diffraction system uses a 5 mW monochromatic laser diode with a wavelength of 780 nm. The light source of the PIDS unit is

a tungsten–halogen lamp which is transmitted in three wavelengths (450, 600, and 900 nm) through a horizontal and vertical polarizer (Beckman Coulter, 2011). The samples were dispersed with distilled water and dissolved sodium pyrophosphate ( $0.5 \text{ g L}^{-1}$ ) and treated for 1 min in an external ultrasonic bath (160 W). Thereafter, the samples were dropwise added to the measuring device with a 3 mL disposable pipette until a suitable measuring concentration was reached. The Fraunhofer.rf780d optical model was used to calculate the grain size distribution from the diffraction pattern.

*XRD:* The X-ray diffraction patterns were recorded with a Cubix3 Pharma diffractometer with a X'Celerator detector.  $\text{Cu K}\alpha$  radiation was used to identify the crystal structure of the powders in the  $2\theta$  range from 5° to 100° with a step size of 0.02° and a count time of 40 s.

*BET:* Single-point BET measurements were conducted using a Micromeritics TriStar 3000 with a nitrogen/helium flow (28.6%  $\text{N}_2$ ). The samples were degassed at 150 °C for 20 min before the measurement.

*SEM:* The particles and their morphology were investigated with a "JSM-7600 F" SEM from Jeol. The accelerating voltage was set to 1 kV, and the beam current was 30 pA. A graphite tape was used to attach the samples on the sample holders. EDX measurements were conducted with an equipped X-Max 150 mm<sup>2</sup> detector (Oxford Instruments) and processed with Aztec software. Therefore, the accelerating voltage and beam current were increased to 20 kV and 500 pA, respectively. The cross sections of the cycled electrodes were prepared by embedding in an organic resin and subsequent cutting via microtomy.

*TEM:* The cross-sectional TEM lamellae were cut from an NMC spherical particle covered by alumina. For the investigation of cycled cathodes, the cells were opened under argon atmosphere and the cathodes were washed with ethyl methyl carbonate to remove  $\text{LiPF}_6$ . The cross-sectional cuts of the sample were prepared via focused ion beam (FIB) using a Fei Helios 650 dual-beam FIB device. During the preparation process, carbon and platinum protective layers were deposited on top of the film. The probe aberration-corrected HAADF-STEM and EDX were performed on a probe aberration-corrected Fei Titan3 80-300 electron microscope operated at 300 kV equipped with Super-X EDX detector system. HRTEM images and EELS data were acquired on a double aberration-corrected Fei Titan3 80–300 electron microscope operated at 300 kV in monochromated mode providing an energy resolution of 150 meV. Before the TEM experiments, the specimen was cleaned through plasma cleaning.

*XPS:* XPS measurements were conducted on a cycled cathode in discharged state. The cells were opened under argon atmosphere and the cathode was mounted on the XPS sample holder and transferred to the XPS analysis equipment without any exposure to air. The XPS measurements were conducted on a ESCALAB 250xi system from ThermoFisher Scientific, using an Al  $\text{K}\alpha$  excitation source. The diameter of the measurement spot was 900  $\mu\text{m}$ . Depth profiling was made by argon ion beam sputtering (5 keV). The graphite peak at 284.6 eV was used as a reference for the adjustment of the energy scale in the presented spectra. The resolution of the measurements was in general 0.1 eV.

*Electrode and Cell Preparation:* Electrodes for electrochemical measurements were prepared by blending 90 wt% NMC with 5 wt% PVDF (Solef PVDF 5130) as a binder and 5 wt% Super PLi (Timcal) as a conductive additive under inert gas atmosphere. N-Methyl-2-pyrrolidone (NMP) was used as the solvent. The slurry was casted on aluminum foil (MTI, thickness: 15  $\mu\text{m}$ ) and dried for 20 min on a 120 °C heating plate in air. Afterward, the electrode sheet was dried in a vacuum furnace at 120 °C for 2 h. Circular electrodes with a diameter of 12 mm were punched out, calendered with a pressure of 620 kPa, and dried again in a vacuum furnace at 120 °C for 12 h to remove any residual water and NMP. The cathode loading for all samples was adjusted to 1.3–1.4  $\text{mAh cm}^{-2}$  ( $\approx 7.2$ – $7.8 \text{ mg}_{\text{NMC}} \text{ cm}^{-2}$ , assuming a specific capacity of 180  $\text{mAh g}^{-1}$ ) with a density of the electrodes (calculated by volume and mass of the individual electrodes) of 1.804–1.874  $\text{g cm}^{-3}$ .

For the cycling tests, the cells were assembled as CR2032-type coin cells (MTI Corporation) in an argon-filled glove box (Glovebox Systemtechnik GmbH). Lithium metal (Rockwood Lithium GmbH) is used as the anode material. Celgard 2500 was used as the separator. A solution (25  $\mu\text{L}$ ) of 1 molar  $\text{LiPF}_6$  in ethylene carbonate and ethyl methyl carbonate

(50:50 wt wt<sup>-1</sup>; Sigma-Aldrich) was used as electrolyte. The cells were locked with a crimping (MTI).

**Cell Cycling:** Galvanostatic cycling was performed between 3.0 and 4.3 V versus Li<sup>+</sup>/Li using a MACCOR battery cycler. For the calculation of the capacities and the specific currents, only the mass of the active material was considered. For the coin half-cells during cycling, the C rate was increased every four cycles, starting from 0.1/0.1 (charge/discharge) to 0.3/0.3, 0.5/0.5, 1.0/1.0, 1.0/2.0, and 1.0/4.0 C. Afterward, the cell was cycled at 0.5/0.5 C for long-term stability test. For EIS measurements, the cells were cycled for four cycles at 0.1/0.1 C. Afterward the C rate was increased to 0.5/0.5 C and the cells were cycled for additional 46 cycles.

**EIS:** EIS measurements were performed using an impedance analyzer (VMP300) over the frequency range of 100 mHz to 1 MHz at 4.3 V, state of charge (SOC) = 100%, with an AC voltage of 10 mV amplitude.

## Supporting Information

Supporting Information is available from the Wiley Online Library or from the author.

## Acknowledgements

The authors would like to thank Erik Peldszus and Steve Rienecker for the support with scanning electron microscopy and X-ray photoelectron spectroscopy analysis. The Qu-Ant-EM microscope and the direct electron detector were partly funded by the Hercules fund from the Flemish Government. N.G. and J.V. acknowledge funding from GOA project "Solarpaint" of the University of Antwerp. Funding from the Flemish Research Fund (FWO) project G0F1320N is acknowledged.

Open access funding enabled and organized by Projekt DEAL.

## Conflict of Interest

The authors declare no conflict of interest.

## Data Availability Statement

Data available on request from the authors.

## Keywords

alumina coating, degradation, dry coating, fumed metal oxides, lithium-ion batteries, NMC cathode materials, nanostructured oxide

Received: January 20, 2021

Published online: February 24, 2021

- [1] T. Li, X. Li, Z. Wang, H. Guo, *J. Power Sources* **2017**, 342, 495.
- [2] W. Liu, P. Oh, X. Liu, M.-J. Lee, W. Cho, S. Chae, Y. Kim, J. Cho, *Angew. Chem. Int. Ed.* **2015**, 54, 4440.
- [3] Y. Oh, S. Nam, S. Wi, S. Hong, B. Park, *Electron. Mater. Lett.* **2012**, 8, 91.
- [4] L. de Biasi, A. O. Kondrakov, H. Geßwein, T. Brezesinski, P. Hartmann, J. Janek, *J. Phys. Chem. C* **2017**, 121, 26163.
- [5] K. Shizuka, T. Kobayashi, K. Okahara, K. Okamoto, S. Kanzaki, R. Kanno, *J. Power Sources* **2005**, 146, 589.
- [6] S.-K. Jung, H. Gwon, J. Hong, K.-Y. Park, D.-H. Seo, H. Kim, J. Hyun, W. Yang, K. Kang, *Adv. Energy Mater.* **2014**, 4, 1300787.
- [7] L. de Biasi, B. Schwarz, T. Brezesinski, P. Hartmann, J. Janek, H. Ehrenberg, *Adv. Mater.* **2019**, 31, 1900985.
- [8] B. Wu, J. Bi, Q. Liu, D. Mu, L. Wang, J. Fu, F. Wu, *Electrochim. Acta* **2019**, 298, 609.
- [9] K.-S. Lee, S.-T. Myung, K. Amine, H. Yashiro, Y.-K. Sun, *J. Electrochem. Soc.* **2007**, 154, A971.
- [10] S.-M. Bak, E. Hu, Y. Zhou, X. Yu, S. D. Senanayake, S.-J. Cho, K.-B. Kim, K. Y. Chung, X.-Q. Yang, K.-W. Nam, *ACS Appl. Mater. Interfaces* **2014**, 6, 22594.
- [11] T. Li, X.-Z. Yuan, L. Zhang, D. Song, K. Shi, C. Bock, *Electrochem. Energy Rev.* **2020**, 3, 43.
- [12] J. Duan, X. Tang, H. Dai, Y. Yang, W. Wu, X. Wei, Y. Huang, *Electrochem. Energy Rev.* **2020**, 3, 1.
- [13] D. Mohanty, K. Dahlberg, D. M. King, L. A. David, A. S. Sefat, D. L. Wood, C. Daniel, S. Dhar, V. Mahajan, M. Lee, F. Albano, *Sci. Rep.* **2016**, 6, 26532.
- [14] S. Schweidler, L. de Biasi, G. Garcia, A. Mazilkin, P. Hartmann, T. Brezesinski, J. Janek, *ACS Appl. Energy Mater.* **2019**, 2, 7375.
- [15] A. Mauger, C. Julien, *Ionics* **2014**, 20, 751.
- [16] G. E. Blomgren, *J. Electrochem. Soc.* **2017**, 164, A5019.
- [17] X. Xiong, Z. Wang, G. Yan, H. Guo, X. Li, *J. Power Sources* **2014**, 245, 183.
- [18] J. Cabana, B. J. Kwon, L. Hu, *Acc. Chem. Res.* **2018**, 51, 299.
- [19] Y. J. Kim, J. Cho, T.-J. Kim, B. Park, *J. Electrochem. Soc.* **2003**, 150, A1723.
- [20] J. L. Tebbe, A. M. Holder, C. B. Musgrave, *ACS Appl. Mater. Interfaces* **2015**, 7, 24265.
- [21] J. Zheng, P. Yan, J. Zhang, M. H. Engelhard, Z. Zhu, B. J. Polzin, S. Trask, J. Xiao, C. Wang, J. Zhang, *Nano Res.* **2017**, 10, 4221.
- [22] N. Nitta, F. Wu, J. T. Lee, G. Yushin, *Mater. Today* **2015**, 18, 252.
- [23] D. Zuo, G. Tian, X. Li, D. Chen, K. Shu, *J. Alloys Compd.* **2017**, 706, 24.
- [24] B. Xiao, X. Sun, *Adv. Energy Mater.* **2018**, 8, 1802057.
- [25] P. Zhou, Z. Zhang, H. Meng, Y. Lu, J. Cao, F. Cheng, Z. Tao, J. Chen, *Nanoscale* **2016**, 8, 19263.
- [26] R. Jung, R. Morasch, P. Karayaylali, K. Phillips, F. Maglia, C. Stinner, Y. Shao-Horn, H. A. Gasteiger, *J. Electrochem. Soc.* **2018**, 165, A132.
- [27] T. Hatsukade, A. Schiele, P. Hartmann, T. Brezesinski, J. Janek, *ACS Appl. Mater. Interfaces* **2018**, 10, 38892.
- [28] W. Cho, S.-M. Kim, K.-W. Lee, J. H. Song, Y. N. Jo, T. Yim, H. Kim, J.-S. Kim, Y.-J. Kim, *Electrochim. Acta* **2016**, 198, 77.
- [29] H. Lee, Y. Kim, Y.-S. Hong, Y. Kim, M. G. Kim, N.-S. Shin, J. Cho, *J. Electrochem. Soc.* **2006**, 153, A781.
- [30] K. Yang, L.-Z. Fan, J. Guo, X. Qu, *Electrochim. Acta* **2012**, 63, 363.
- [31] S. J. Shi, J. P. Tu, Y. J. Mai, Y. Q. Zhang, Y. Y. Tang, X. L. Wang, *Electrochim. Acta* **2012**, 83, 105.
- [32] Y. Xie, D. Gao, L. L. Zhang, J. J. Chen, S. Cheng, H. F. Xiang, *Ceram. Int.* **2016**, 42, 14587.
- [33] Z. Yang, Q. Qiao, W. Yang, *Electrochimica Acta* **2011**, 56, 4791.
- [34] H. J. Lee, Y. J. Park, *Solid State Ion.* **2013**, 230, 86.
- [35] J.-H. Shim, K.-S. Lee, A. Missyul, J. Lee, B. Linn, E. C. Lee, S. Lee, *Chem. Mater.* **2015**, 27, 3273.
- [36] S.-B. Kim, K. J. Lee, W. J. Choi, W.-S. Kim, I. C. Jang, H. H. Lim, Y. S. Lee, *J. Solid State Electrochem.* **2010**, 14, 919.
- [37] S.-W. Cho, K.-S. Ryu, *Mater. Chem. Phys.* **2012**, 135, 533.
- [38] Z. Chen, Z. Zhang, P. Liu, S. Wang, W. Zhang, D. Chen, *J. Alloys Compd.* **2019**, 780, 643.
- [39] L. Zou, Y. Zhang, F. Wang, B. Zhou, Z. Wang, *Integr. Ferroelectr.* **2013**, 147, 103.
- [40] W. Luo, B. Zheng, J. He, *J. Alloys Compd.* **2017**, 705, 405.
- [41] C. Chen, T. Tao, W. Qi, H. Zeng, Y. Wu, B. Liang, Y. Yao, S. Lu, Y. Chen, *J. Alloys Compd.* **2017**, 709, 708.
- [42] M. R. Laskar, D. H. K. Jackson, S. Xu, R. J. Hamers, D. Morgan, T. F. Kuech, *ACS Appl. Mater. Interfaces* **2017**, 9, 11231.
- [43] K. S. Yoo, Y. H. Kang, K. R. Im, C.-S. Kim, *Materials* **2017**, 10, 1273.

- [44] Y. Chen, Y. Zhang, B. Chen, Z. Wang, C. Lu, *J. Power Sources* **2014**, 256, 20.
- [45] A. Yano, A. Ueda, M. Shikano, H. Sakaebe, Z. Ogumi, *J. Electrochem. Soc.* **2016**, 163, A75.
- [46] J.-Z. Kong, C. Ren, G.-A. Tai, X. Zhang, A.-D. Li, D. Wu, H. Li, F. Zhou, *J. Power Sources* **2014**, 266, 433.
- [47] K. Min, K. Park, S. Y. Park, S.-W. Seo, B. Choi, E. Cho, *J. Electrochem. Soc.* **2018**, 165, A79.
- [48] S. Dong, Y. Zhou, C. Hai, J. Zeng, Y. Sun, Y. Shen, X. Li, X. Ren, G. Qi, X. Zhang, L. Ma, *Ceram. Int.* **2019**, 45, 144.
- [49] Z. Chen, Y. Qin, K. Amine, Y.-K. Sun, *J. Mater. Chem.* **2010**, 20, 7606.
- [50] M. Aykol, S. Kirklın, C. Wolverton, *Adv. Energy Mater.* **2014**, 4, 1400690.
- [51] H. Ye, Y.-X. Yin, S.-F. Zhang, Y. Shi, L. Liu, X.-X. Zeng, R. Wen, Y.-G. Guo, L.-J. Wan, *Nano Energy* **2017**, 36, 411.
- [52] S. Neudeck, F. Strauss, G. Garcia, H. Wolf, J. Janek, P. Hartmann, T. Brezesinski, *Chem. Commun.* **2019**, 55, 2174.
- [53] S. Neudeck, A. Mazilkin, C. Reitz, P. Hartmann, J. Janek, T. Brezesinski, *Sci. Rep.* **2019**, 9, 1.
- [54] R. Pfeffer, R. N. Dave, D. Wei, M. Ramlakhan, *Powder Technol.* **2001**, 117, 40.
- [55] D. N. Goldstein, J. A. McCormick, S. M. George, *J. Phys. Chem. C* **2008**, 112, 19530.
- [56] R. L. Puurunen, *J. Appl. Phys.* **2005**, 97, 121301.
- [57] S.-H. Lee, C. S. Yoon, K. Amine, Y.-K. Sun, *J. Power Sources* **2013**, 234, 201.
- [58] J.-T. Son, *J. Korean Electrochem. Soc.* **2010**, 13, 246.
- [59] J. Yang, A. Sliva, A. Banerjee, R. N. Dave, R. Pfeffer, *Powder Technol.* **2005**, 158, 21.
- [60] Y. Ouabbas, A. Chamayou, L. Galet, M. Baron, G. Thomas, P. Grosseau, B. Guilhot, *Powder Technol.* **2009**, 190, 200.
- [61] F. Cavallès, R. Sescousse, A. Chamayou, L. Galet, *Adv. Powder Technol.* **2017**, 28, 2875.
- [62] G. Lefebvre, L. Galet, A. Chamayou, *Powder Technol.* **2011**, 208, 372.
- [63] L. Zheng, T. D. Hatchard, M. N. Obrovac, *MRS Commun.* **2019**, 9, 245.
- [64] P. Albers, M. Maier, M. Reisinger, B. Hannebauer, R. Weinand, *Cryst. Res. Technol.* **2015**, 50, 846.
- [65] B. Han, B. Key, S. H. Lapidus, J. C. Garcia, H. Iddir, J. T. Vaughey, F. Dogan, *ACS Appl. Mater. Interfaces* **2017**, 9, 41291.
- [66] S.-I. Lee, U.-H. Jung, Y.-S. Kim, M.-H. Kim, D.-J. Ahn, H.-S. Chun, *Korean J. Chem. Eng.* **2002**, 19, 638.
- [67] S. G. Stewart, J. Newman, *J. Electrochem. Soc.* **2008**, 155, F13.
- [68] S. C. Jung, Y.-K. Han, *J. Phys. Chem. Lett.* **2013**, 4, 2681.
- [69] J. Uhlendorf, B. Ruprecht, E. Witt, C. V. Chandran, L. Dörrer, E. Hüger, F. Strauß, P. Heitjans, H. Schmidt, *Z. Für Phys. Chem.* **2017**, 231.
- [70] J. Liu, Q. Wang, B. Rejeeja-jayan, A. Manthiram, *Electrochem. Commun.* **2010**, 12, 750.
- [71] S. J. Shi, Y. J. Mai, Y. Y. Tang, C. D. Gu, X. L. Wang, J. P. Tu, *Electrochim. Acta* **2012**, 77, 39.
- [72] S. J. Shi, J. P. Tu, Y. Y. Tang, X. Y. Liu, Y. Q. Zhang, X. L. Wang, C. D. Gu, *Electrochim. Acta* **2013**, 88, 671.
- [73] Y. Shi, M. Zhang, D. Qian, Y. S. Meng, *Electrochim. Acta* **2016**, 203, 154.
- [74] L. Wang, Y. Ma, P. Wang, S. Lou, X. Cheng, P. Zuo, C. Du, Y. Gao, G. Yin, *J. Electrochem. Soc.* **2017**, 164, A1924.
- [75] L. Li, Z. Chen, Q. Zhang, M. Xu, X. Zhou, H. Zhu, K. Zhang, *J. Mater. Chem. A* **2015**, 3, 894.
- [76] A. Y. Shenouda, H. K. Liu, *J. Alloys Compd.* **2009**, 477, 498.
- [77] S. Vasu, M. B. Sahana, C. Sudakar, R. Gopalan, G. Sundararajan, *Electrochim. Acta* **2017**, 251, 363.
- [78] C. Yang, X. Zhang, J. Huang, P. Ao, G. Zhang, *Electrochim. Acta* **2016**, 196, 261.
- [79] J. Ni, H. Zhou, J. Chen, X. Zhang, *Electrochim. Acta* **2008**, 53, 3075.
- [80] Y. Yang, R. Xu, K. Zhang, S. Lee, L. Mu, P. Liu, C. K. Waters, S. Spence, Z. Xu, C. Wei, D. J. Kautz, Q. Yuan, Y. Dong, Y.-S. Yu, X. Xiao, H.-K. Lee, P. Pianetta, P. Cloetens, J.-S. Lee, K. Zhao, F. Lin, Y. Liu, *Adv. Energy Mater.* **2019**, 9, 1900674.
- [81] H.-H. Ryu, K.-J. Park, C. S. Yoon, Y.-K. Sun, *Chem. Mater.* **2018**, 30, 1155.
- [82] D.-W. Jun, C. S. Yoon, U.-H. Kim, Y.-K. Sun, *Chem. Mater.* **2017**, 29, 5048.
- [83] P. Yan, J. Zheng, J.-G. Zhang, C. Wang, *Nano Lett.* **2017**, 17, 3946.
- [84] A. M. Andersson, D. P. Abraham, R. Haasch, S. MacLaren, J. Liu, K. Amine, *J. Electrochem. Soc.* **2002**, 149, A1358.
- [85] A. M. Andersson, M. Herstedt, A. G. Bishop, K. Edström, *Electrochim. Acta* **2002**, 47, 1885.
- [86] K. Kanamura, H. Tamura, S. Shiraishi, Z.-I. Takehara, **1995**, 40, 913.
- [87] A. M. Andersson, K. Edström, *J. Electrochem. Soc.* **2001**, 148, A1100.
- [88] R. Naejus, D. Lemordant, R. Coudert, P. Willmann, *J. Fluorine Chem.* **1998**, 90, 81.
- [89] R. Dedryvère, S. Laruelle, S. Grugeon, L. Gireaud, J.-M. Tarascon, D. Gonbeau, *J. Electrochem. Soc.* **2005**, 152, A689.
- [90] W. Hetaba, A. Mogilatenko, W. Neumann, *Micron* **2010**, 41, 479.
- [91] L. Bodenes, A. Darwiche, L. Monconduit, H. Martinez, *J. Power Sources* **2015**, 273, 14.
- [92] X.-G. Sun, C. Liao, L. Baggetto, B. Guo, R. R. Unocic, G. M. Veith, S. Dai, *J. Mater. Chem. A* **2014**, 2, 7606.
- [93] K. Edström, T. Gustafsson, J. O. Thomas, *Electrochim. Acta* **2004**, 50, 397.
- [94] Q. Wang, L. Jiang, Y. Yu, J. Sun, *Nano Energy* **2019**, 55, 93.
- [95] D. Mandal, K. J. Kim, J. S. Lee, *Langmuir* **2012**, 28, 10310.
- [96] X. Li, J. Liu, B. Wang, M. N. Banis, B. Xiao, R. Li, T.-K. Sham, X. Sun, *RSC Adv.* **2014**, 4, 27126.
- [97] X. Xiao, P. Lu, D. Ahn, *Adv. Mater.* **2011**, 23, 3911.
- [98] C. S. Seu, V. K. Davis, J. Pasalic, R. V. Bugga, *J. Electrochem. Soc.* **2015**, 162, A2259.
- [99] S.-Y. Kim, Y. Qi, *J. Electrochem. Soc.* **2014**, 161, F3137.
- [100] J. S. Park, X. Meng, J. W. Elam, S. Hao, C. Wolverton, C. Kim, J. Cabana, *Chem. Mater.* **2014**, 26, 3128.
- [101] W. Liu, X. Li, D. Xiong, Y. Hao, J. Li, H. Kou, B. Yan, D. Li, S. Lu, A. Koo, K. Adair, X. Sun, *Nano Energy* **2018**, 44, 111.